

Pitch Angle of Galactic Spiral Arms

Shugo Michikoshi¹ and Eiichiro Kokubo²

smichiko@mail.doshisha.ac.jp and kokubo@th.nao.ac.jp

ABSTRACT

One of the key parameters that characterize spiral arms in disk galaxies is a pitch angle that measures the inclination of a spiral arm to the direction of galactic rotation. The pitch angle differs from galaxy to galaxy, which suggests that the rotation law of galactic disks determines it. In order to investigate the relation between the pitch angle of spiral arms and the shear rate of galactic differential rotation, we perform local N -body simulations of pure stellar disks. We find that the pitch angle increases with the epicycle frequency and decreases with the shear rate and obtain the fitting formula. This dependence is explained by the swing amplification mechanism.

Subject headings: galaxies: kinematics and dynamics, galaxies:spiral, method:numerical

1. Introduction

Spiral structures are ubiquitous in various astrophysical disks. In spiral galaxies, there are distinct spiral arm structures. Grand-design spiral galaxies have long continuous symmetric arms, while flocculent spiral galaxies have patchy irregular spiral arms. In a protoplanetary gas disk, gravitational instability can occur during some phase of its evolution, which can produce spiral arms (Gammie 2001). Also in Saturn's rings, the spiral structures in a broad sense exist. The azimuthal brightness asymmetry is observed in the rings (e.g., French et al. 2007), which indicates the existence of the small scale spiral structures called as self-gravity wakes observed in N -body simulations (Salo 1992, 1995). The wakes are caused by the gravitational instability of the ring.

Our understanding of the origin of spiral arms in galaxies is still incomplete. One of the theories to explain spiral arms in galaxies is the density wave theory (Lin & Shu 1964, 1966). Spiral structures are considered as a quasi-stationary standing wave pattern that rotates around the galactic center with a constant pattern speed. The spiral arms may be excited by tidal interactions with companion galaxies (e.g., Oh et al. 2008) or the central bars (e.g., Buta et al. 2005; Salo & Schmidt 2010).

¹ Department of Environmental Systems Science, Doshisha University, Tatara Miyakodani 1-3, Kyotanabe City, Kyoto 610-0394, Japan

² Division of Theoretical Astronomy, National Astronomical Observatory of Japan, Osawa, Mitaka, Tokyo 181-8588, Japan

In a differentially rotating disk, a leading density pattern rotates to a trailing one due to the shear. If Toomre’s Q value is larger than unity but not too much, the amplitude of the pattern can be enhanced during the rotation. This mechanism is called swing amplification (Goldreich & Lynden-Bell 1965; Julian & Toomre 1966; Toomre 1981). If a perturber such as the corotating over-dense region exists, trailing patterns form (Julian & Toomre 1966). In N -body simulations, since a disk consists of a finite number of stars, small density noise always exists. Thus, even if there is not a perturber, the small leading wave always exists, and the trailing wave can grow spontaneously due to the swing amplification mechanism (Toomre & Kalnajs 1991). The spirals generated by the swing amplification are not stationary but transient and recurrent, which appear and disappear continuously. This transient and recurrent picture is supported by N -body simulations for multi-arm spirals (Sellwood & Carlberg 1984; Baba et al. 2009; Sellwood 2000, 2010; Fujii et al. 2011).

The linear theory of the swing amplification gives the amplification factor and the most unstable wavelength, but it cannot explain the overall evolution of spiral arms. Baba et al. (2013) studied the dynamics of stars in spiral arms and found that the nonlinear particle wave interaction is important to understand the damping and growing phase of spiral arms. D’Onghia et al. (2013) performed high-resolution N -body simulations including initial density inhomogeneities that induce the spiral patterns due to the swing amplification. Once spiral arms form, the spiral arms remain. This results from the nonlinear effect. The local underdense and overdense regions act as perturbers, which maintain the spiral structure.

One of the key parameters to characterize the morphology of spiral galaxies is the pitch angle. The pitch angle is the angle between the tangents to a spiral arm and a perfect circle, which measures how tightly the spiral arms are wound. Julian & Toomre (1966) investigated the response of the particle density to an imposed perturbation using the collisionless Boltzmann equation. They found the trend that the pitch angle decreases with the shear rate. The correlation between the shear rate and the pitch angle enables us to determine a rotation curve from the spiral structure.

The epicycle frequency κ is related to the shear rate Γ :

$$\Gamma = \frac{2A}{\Omega} = -\frac{d \log \Omega}{d \log R} = 2 - \frac{\kappa^2}{2\Omega^2}, \quad (1)$$

where A is the first Oort constant, and Ω is the circular frequency. The observational study shows the relation that the pitch angle decreases with the shear rate, and the fitting formula is given as (Seigar et al. 2005, 2006):

$$\theta = (64.25 \pm 2.87)^\circ - \Gamma(36.62 \pm 2.77)^\circ. \quad (2)$$

Grand et al. (2013) performed global N -body simulations and investigated the spiral patterns using Fourier analysis. From the spiral phase variation they calculated the pitch angle of the spiral arm. They found that galaxies of the higher shear rate have the smaller pitch angle. They did

not study the dependence of the pitch angle on Toomre’s Q value since Q evolves over time. It is expected that the pitch angle barely depends on Q from Julian & Toomre (1966).

In order to understand the dynamics of spiral arms, we investigate the pitch angle dependence on the shear rate by local N -body simulations of pure stellar disks. Section 2 summarizes the calculation method. In Section 3, we present the simulation results. In Section 4, we discuss the relation between the pitch angle and the shear rate by using the linear theory. Section 5 gives a summary.

2. Calculation Method

2.1. Model

We perform local N -body simulations of pure stellar disks based on the epicycle approximation. We do not consider an entire disk but a small rotating patch by employing a local shearing box (e.g., Toomre & Kalnajs 1991; Fuchs et al. 2005). This treatment reduces the number of necessary particles in a simulation significantly, and enables us to perform high resolution simulations. We consider a small patch of a disk such that $L_x, L_y \ll r$, where L_x and L_y are the width and length of the patch and r is the galactocentric distance of the patch. We adopt a local Cartesian coordinate system (x, y, z) , whose origin revolves around the galactic center with the circular frequency Ω , which is given by

$$\Omega^2 = \frac{1}{r} \left(\frac{\partial \Phi}{\partial r} \right), \quad (3)$$

where Φ is the axisymmetric galactic potential. The x -axis is directed radially outward, the y -axis is parallel to the direction of rotation, and the z -axis is normal to the x - y plane. In the epicycle approximation, neglecting the higher order terms with respect to x , y , and z , the equation of motion of particle i is given by

$$\begin{aligned} \frac{d^2 x_i}{dt^2} &= 2\Omega \frac{dy_i}{dt} + (4\Omega^2 - \kappa^2) x_i + \sum_{j \neq i} \frac{Gm(x_j - x_i)}{(r_{ij}^2 + \epsilon^2)^{3/2}}, \\ \frac{d^2 y_i}{dt^2} &= -2\Omega \frac{dx_i}{dt} + \sum_{j \neq i} \frac{Gm(y_j - y_i)}{(r_{ij}^2 + \epsilon^2)^{3/2}}, \\ \frac{d^2 z_i}{dt^2} &= -\nu^2 z_i + \sum_{j \neq i} \frac{Gm(z_j - z_i)}{(r_{ij}^2 + \epsilon^2)^{3/2}}, \end{aligned} \quad (4)$$

where r_{ij} is the distance between particles i and j , m is the particle mass (e.g., Toomre 1981; Toomre & Kalnajs 1991; Kokubo & Ida 1992; Fuchs et al. 2005). In Equation (4), $2\Omega dy_i/dt$ and $-2\Omega dx_i/dt$ are Coriolis force, $4\Omega^2 x_i$ is the centrifugal force, $-\kappa^2 x_i$ and $-\nu^2 z_i$ are the galactic gravitational force, and the terms proportional to $(r_{ij}^2 + \epsilon^2)^{-3/2}$ are the gravitational force from the other particles. We assume that all particles have the same mass. The length ϵ is the softening

parameter $\epsilon = r_t/4$ where r_t is the tidal radius of a particle:

$$r_t = \left(\frac{2mG}{4\Omega^2 - \kappa^2} \right)^{1/3}. \quad (5)$$

The frequencies κ and ν are the epicycle and vertical frequencies at the center of the computational box:

$$\kappa^2 = \frac{1}{r} \left(\frac{\partial \Phi}{\partial r} \right) + 4\Omega^2, \quad (6)$$

$$\nu^2 = \frac{\partial^2 \Phi}{\partial z^2}. \quad (7)$$

Since the size of the computational box is small, we can assume that all particles in the computational box have the same κ and ν .

The motion of particles is pursued only in the computational box with the periodic boundary condition (Wisdom & Tremaine 1988). There are copied boxes around the computational box. When a particle in the computational box crosses the boundary, the corresponding particle in the copied box comes into the computational box through the opposite boundary. The position and velocity of the particle that crosses the boundary is calculated by considering the velocity shear.

The size of the computational box L_x and L_y should be sufficiently larger than the characteristic scale of the spiral arms that is the critical wavelength of the gravitational instability

$$\lambda_{\text{cr}} = \frac{4\pi^2 G \Sigma_0}{\kappa^2}, \quad (8)$$

where Σ_0 is the initial surface density. We set the size of the computational box as $L_x = L_y = L = 5\lambda_{\text{cr}}$.

We set the unit time as Ω^{-1} and the unit length as r_t (Kokubo & Ida 1992). The equation of motion is integrated using a second-order leapfrog integrator with time-step $\Delta t = (2\pi/\Omega)/200$. We calculate the self-gravity of particles not only in the computational box but also from the surrounding copied boxes. The cutoff length of the gravity is $L_{\text{cut}} = \min(L_x, L_y)$. The self-gravity of particles, which is the most computationally expensive part, is calculated using the special-purpose computer, GRAPE-7 (Kawai & Fukushima 2006).

2.2. Initial Conditions

We assume that the initial surface density Σ_0 of particles in the computational box is uniform. The total mass in area λ_{cr}^2 is fixed and the particle mass is given by $m = \lambda_{\text{cr}}^2 \Sigma_0 / N_c$ where N_c is the number of particles in λ_{cr}^2 . We set $N_c = 8000$ and then the total number of particles is $N = N_c L_x L_y / \lambda_{\text{cr}}^2 = 2.0 \times 10^5$. If we neglect the weak dependence of the Coulomb logarithm on N_c

and assume $\log \Lambda \simeq 5$, the two-body relaxation time is proportional to N_c , which is estimated as (e.g., Kokubo & Ida 1992)

$$t_r \simeq 2 \times 10^2 (Q/1.4)^4 (N_c/8000) \Omega^{-1}. \quad (9)$$

Since the simulation time is much shorter than the relaxation time, the two-body relaxation barely affects the dynamical evolution.

The initial Toomre's Q value is

$$Q_{\text{ini}} = \frac{\sigma_x \kappa}{3.36 G \Sigma_0}, \quad (10)$$

where σ_x is the initial radial velocity dispersion (Toomre 1964). The initial radial velocity dispersion σ_x is calculated from Q_{ini} . We adopt the triaxial Gaussian model as the velocity distribution. In the epicycle approximation, the ratio of azimuthal to radial velocity dispersions is $\sigma_y/\sigma_x = \kappa/2\Omega$ (e.g., Binney & Tremaine 2008). The ratio of the radial to vertical velocity dispersions σ_z/σ_x depends on κ and σ_z . The ratio σ_z/σ_x increases with κ . For $\sigma_z \lesssim r_t \Omega$, the ratio is $\sigma_z/\sigma_x \sim 0.5\text{--}0.8$ (Ida et al. 1993). We adopt the simple linear model $\sigma_z/\sigma_x = 0.3\kappa/\Omega + 0.2$ for $\sigma_z \lesssim r_t \Omega$. The vertical distribution of particles is determined so that it is consistent with the velocity distribution, and x and y of particles are distributed randomly.

There are 8 parameters κ , ν , Q_{ini} , N_c , L , L_{cut} , ϵ , and Δt in the simulation model. We mainly explore the two parameters, $\tilde{\kappa} = \kappa/\Omega$ and Q_{ini} . We have 50 simulation models (1a–1j, 2a–2j, 3a–3j, 4a–4j, 5a–5j), where $Q_{\text{ini}} = 1.0(1), 1.2(2), \dots$, and $1.8(5)$, and $\tilde{\kappa} = 1.0$ (a), 1.1 (b), \dots , and 1.9 (j), respectively. We have checked that the following results barely depend on the other parameters N_c , L , L_{cut} , ϵ , and Δt . We adopt the vertical frequency $\nu = 3\Omega$. We also have performed the other 50 simulation models with $\nu = \Omega$ and confirmed that the following results barely depend on ν .

3. Pitch Angle

3.1. Spatial Correlation

In order to investigate the pitch angle quantitatively, we calculate the spatial correlation function ξ :

$$\xi(x, y) = -1 + \frac{1}{\Sigma_0^2 L^2} \iint_{-L/2}^{L/2} \Sigma(x+x', y+y') \Sigma(x', y') dx' dy'. \quad (11)$$

We calculate the surface density with the uniform grid of 90×90 . Figure 1a shows the particle surface density distribution at $t = 2.0 \times 2\pi/\Omega$ for model 1a where $\tilde{\kappa} = 1.4$ and $Q_{\text{ini}} = 1.0$. Spiral or wake structures are formed due to gravitational instability. They are trailing, that is, the pitch angle is positive. Figure 1b shows the time-averaged ξ over $3 \times 2\pi/\Omega$. The most prominent feature is the inclined straight line crossing the center, in other words, a trailing pattern. For $Q_{\text{ini}} = 1.4$, the basic features are the same as those for $Q_{\text{ini}} = 1.0$. Figures 1c and 1d show the clear trailing patterns. However their amplitude is smaller than those for $Q_{\text{ini}} = 1.0$. This is because the amplification factor of the swing amplification decreases with Toomre's Q value (Toomre 1981). For $Q_{\text{ini}} = 1.8$,

the wakes are trailing but faint and thus the spatial correlation is very weak (Figure 1e and 1f). The models of $Q_{\text{ini}} = 1.6$ show the similar tendency to those of $Q_{\text{ini}} = 1.8$. The distinct spirals do not form for $Q_{\text{ini}} \gtrsim 1.5$.

We measure the pitch angle from the spatial correlation. The pitch angle is the angle between the vertical line and the correlation ridge that is approximated by the straight line crossing the origin. We define the pitch angle of spirals as the angle θ where the function $f(\theta)$ has the maximum value, where $f(\theta)$ is (Wakita & Sekiya 2008)

$$f(\theta) = \int_{-L/2}^{L/2} \xi(s \sin \theta, -s \cos \theta) ds. \quad (12)$$

The pitch angle dependence on Γ and Q_{ini} is shown in Figure 2. The pitch angle decreases with the shear rate Γ . For the small shear rate, since the winding due to the shear is weak, the pitch angle is large. The pitch angle increases with Q_{ini} , but its dependence is very weak. The shear rate Γ is more important than Q_{ini} . The dashed curve in Figure 2 is calculated from the observational fitting formula of Equation (2) (Seigar et al. 2006). Roughly speaking, Equation (2) agrees with the simulation results. However, the fitting values for $0.6 < \Gamma < 1.2$ are larger than those from the simulations systematically. Furthermore, the observational fitting formula is the linear function of Γ , but as shown in Figure 2, it seems that the pitch angle is a convex function of Γ .

Fuchs (2001) derived an empirical formula of the azimuthal wavenumber of the most amplified wave. Baba et al. (2013) used this empirical formula and assumed that the radial wavelength is equal to the critical wavelength and derived the pitch angle:

$$\tan \theta = 1.932 - 5.186 \left(\frac{\Gamma}{2} \right) + 4.704 \left(\frac{\Gamma}{2} \right)^2. \quad (13)$$

As shown in Figure 2, this pitch angle formula agrees with our results for $0.2 \leq \Gamma \leq 1.0$, but does not for $\Gamma < 0.2$ or $1.0 < \Gamma$. This is mainly caused by the limitation of the fitting formula of the azimuthal wave number of Fuchs (2001), which is applicable only for $0.2 \leq \Gamma \leq 1.0$. In addition, strictly speaking, the radial wavelength can be different from the critical wavelength and depends on the shear rate Γ .

We derive a new formula from the results of the numerical simulations. If we neglect any interactions among particles, the spiral arm swings from leading to trailing due to differential rotation, and the pitch angle evolution is described as (e.g., Binney & Tremaine 2008)

$$\tan \theta = \frac{1}{2At}. \quad (14)$$

If we choose about half an epicycle period $t \simeq 3.5/\kappa$, from Equation (14) we obtain

$$\tan \theta \simeq \frac{1}{7} \frac{\kappa}{A} = \frac{4}{7} \frac{\tilde{\kappa}}{4 - \tilde{\kappa}^2} = \frac{2}{7} \frac{\sqrt{4 - 2\Gamma}}{\Gamma}. \quad (15)$$

The solid curve in Figure 2 corresponds to the pitch angle given by Equation (15), which agrees well with the results of the simulations.

It is not trivial that Equation (14) with $t \simeq 3.5/\kappa$ gives the pitch angle of spiral arms. In Section 4, we discuss the derivation of the pitch angle formula from the linear analysis.

3.2. Fourier Transformation

We can extract the dominant wave mode using the Fourier analysis. The Fourier transformation of the surface density is defined by

$$\hat{\Sigma}(k_x, k_y) = \iint \Sigma(x, y) \exp(i(k_x x + k_y y)) dk_x dk_y, \quad (16)$$

where k_x and k_y are the radial and azimuthal wavenumbers.

Figure 3 shows the time-averaged Fourier amplitude over $3 \times \Omega/2\pi$ for $\tilde{\kappa} = 1.4$ and $Q_{\text{ini}} = 1.0, 1.4,$ and 1.8 (models 1e, 3e, and 5e). In these models the Fourier amplitude has the maximum at $(k_x, k_y) \simeq (1.0k_{\text{cr}}, 0.5k_{\text{cr}})$. The wavenumber of the dominant mode does not depend on Q_{ini} . However, the amplitude of the wave depends on Q_{ini} . As Q_{ini} increases, the maximum amplitude decreases. For large Q_{ini} , the peak position is obscure.

The pitch angle of the wave with (k_x, k_y) is

$$\tan \theta = \frac{k_y}{k_x}. \quad (17)$$

The spiral arm corresponds to the dominant wave whose amplitude is the maximum. We can calculate the pitch angle of the spiral arm from Equation (17) using the wavenumber of the dominant wave. We compare the pitch angle from the Fourier transformation with that from the correlation function. Figure 4 shows the pitch angle from the Fourier transformation. For $Q_{\text{ini}} < 1.5$, the pitch angle from the Fourier transformation is the same as those from the spatial correlation.

However, if $Q_{\text{ini}} = 1.6,$ and 1.8 and $\Gamma < 1.0$, we can see the difference of the pitch angle. For $\Gamma < 0.4$, we cannot obtain the pitch angle of the trailing wave because the amplitude of the wave is too small to extract the dominant mode for $Q_{\text{ini}} = 1.6$ and 1.8 . The extraction of the dominant wave mode by the Fourier analysis fails. In these parameters, the correlation method gives the more accurate pitch angle than the Fourier analysis.

4. Linear Analysis

In the swing amplification mechanism, while the wavelet rotates from leading to trailing due to the shear, the wavelet is amplified. Thus, the initial leading wavelet is necessary. Since the number of particles is finite, the Poisson noise implies the leading mode that has the small amplitude.

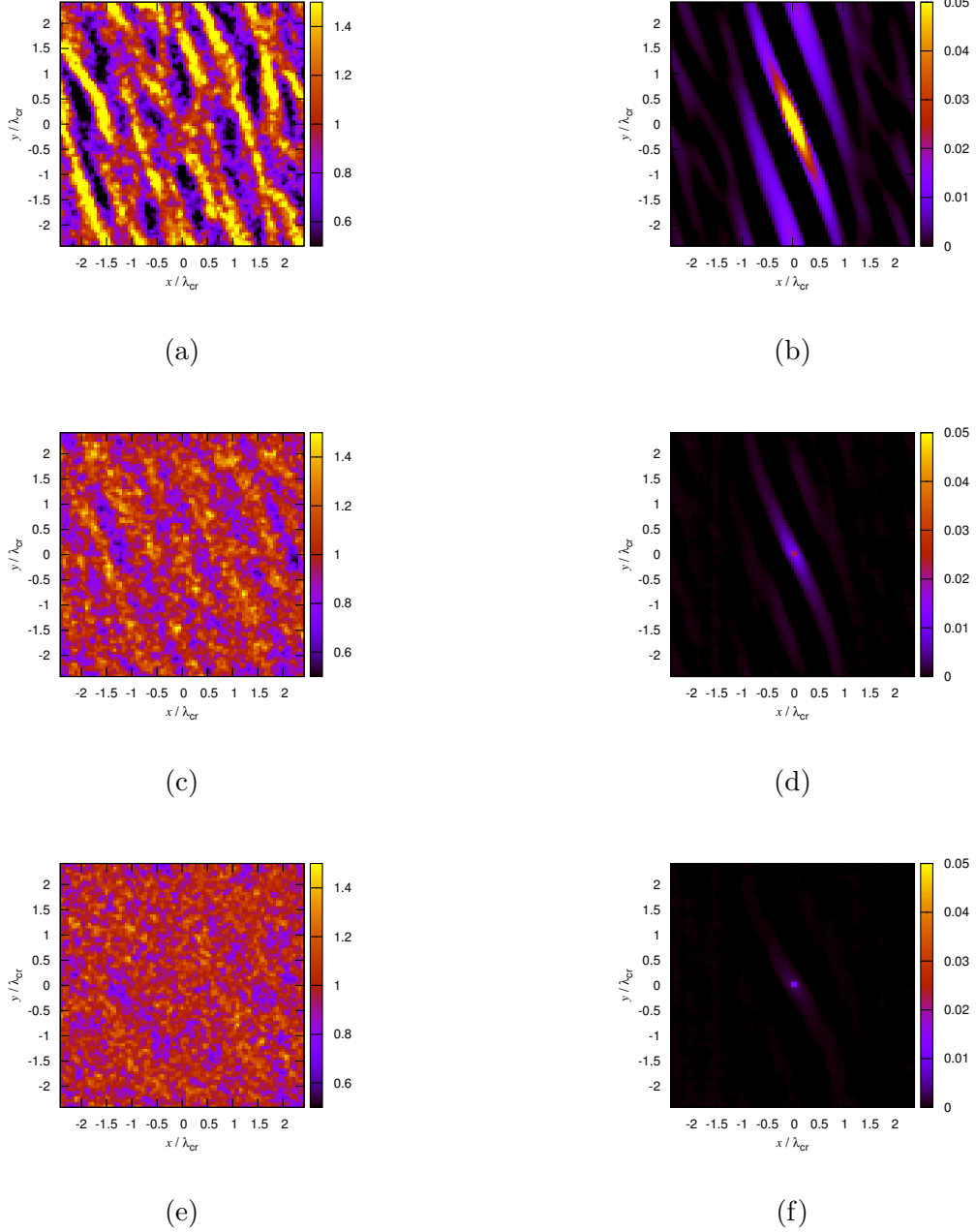


Fig. 1.— The surface density distribution in the x - y plane (left panels) at $t = 2.0 \times 2\pi/\Omega$ and the time-averaged spatial correlation (right panels) for $Q = 1.0$ (model 1e) (top panels) and $Q = 1.4$ (model 3e) (middle panels) and $Q = 1.8$ (model 5e) (bottom panels). The epicycle frequency of all models is $\tilde{\kappa} = 1.4$. The surface density is normalized by the average initial surface density.

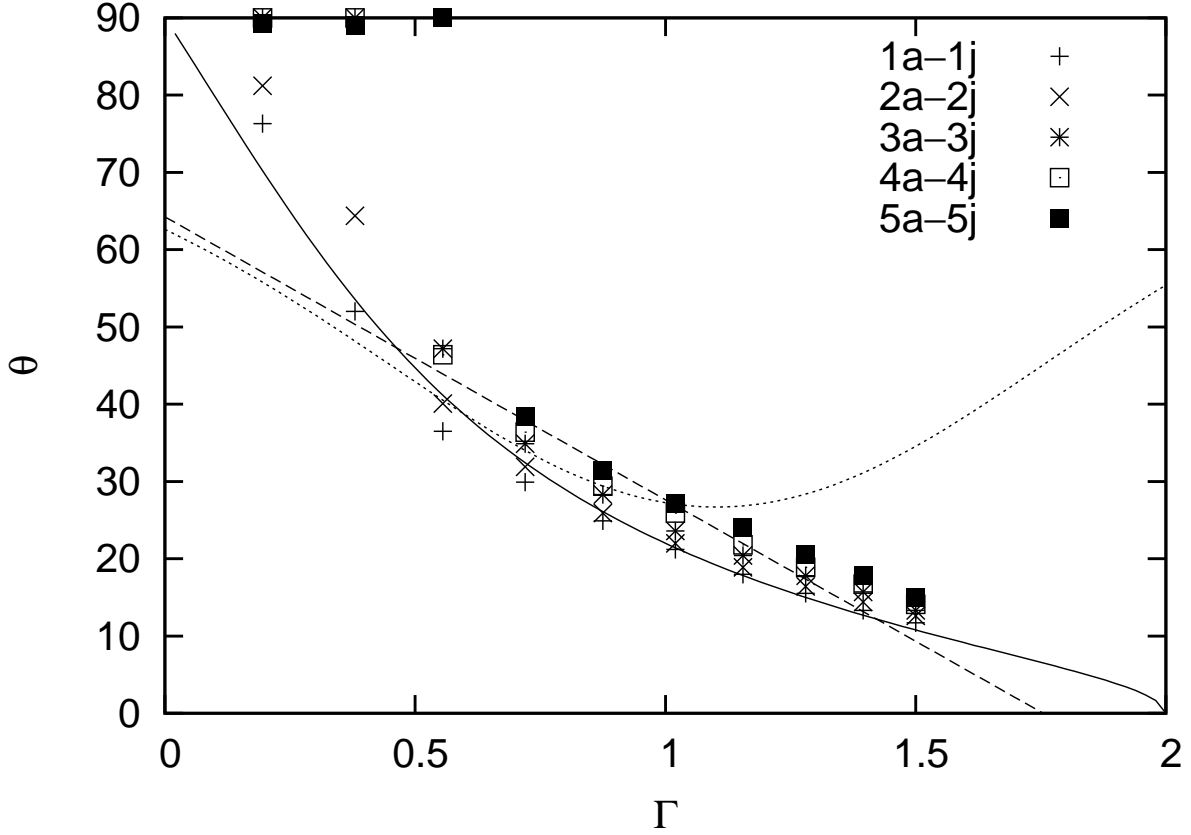


Fig. 2.— The pitch angle θ as a function of Γ for the initial Q values 1.0, 1.2, 1.4, 1.6, and 1.8. The solid curve shows the fitting formula described by Equation (15), and the dashed curve corresponds to the observational fitting given by Equation (2) (Seigar et al. 2006). The dotted line is the formula proposed by the linear theory for $0.2 \leq \Gamma \leq 1.0$ (Fuchs 2001; Baba et al. 2013).

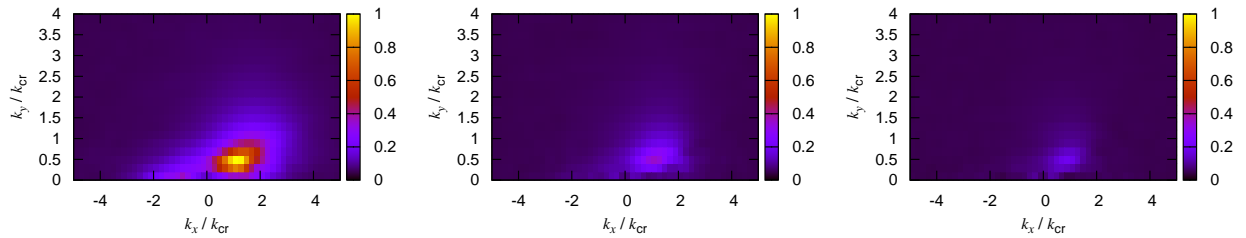


Fig. 3.— The time-averaged Fourier amplitude $|\hat{\Sigma}|$ for $\tilde{\kappa} = 1.4$, $Q_{\text{ini}} = 1.0, 1.4, 1.8$ (models 1e, 3e, 5e) (left, middle, right panels, respectively). The wavenumber is normalized by $k_{\text{cr}} = 2\pi/\lambda_{\text{cr}}$.

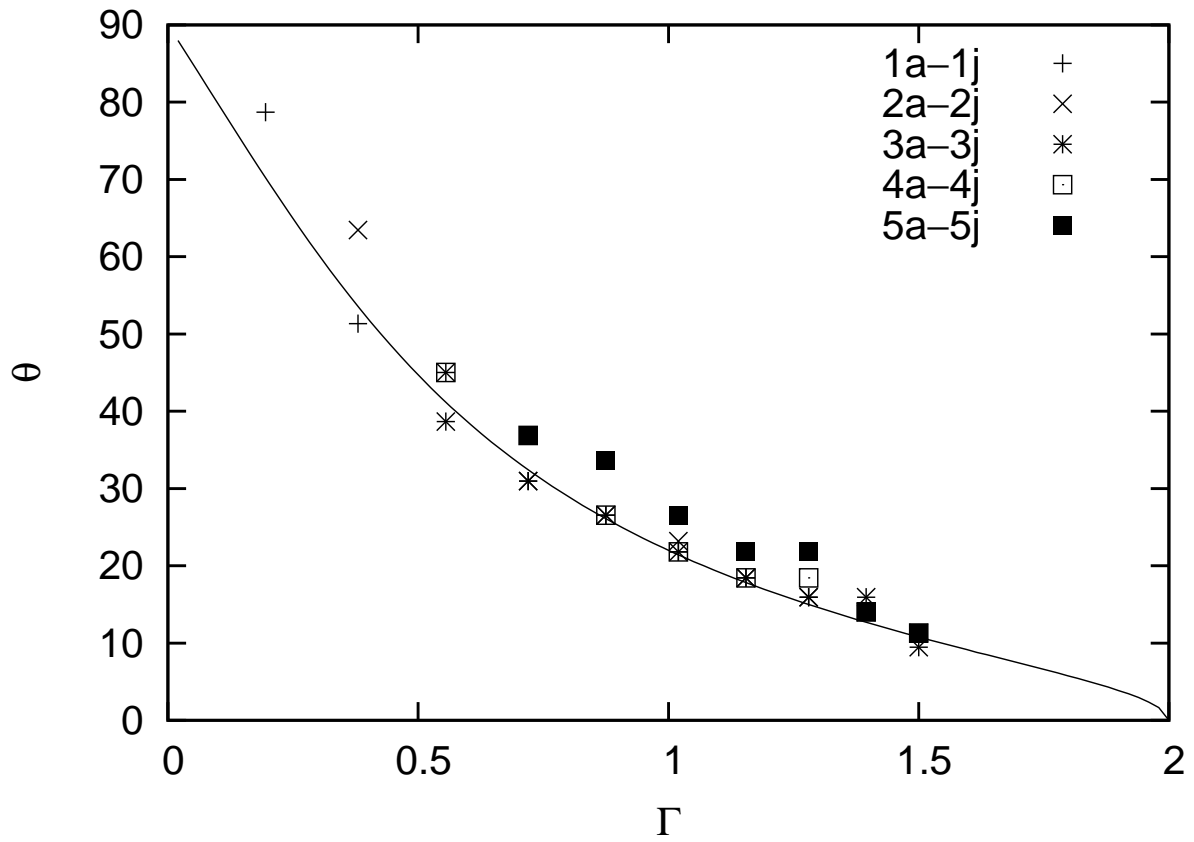


Fig. 4.— The same as Figure 2 but the pitch angle is calculated from the Fourier transformation.

After the first spiral arms are formed, the activity of the rapid spiral formation and destruction continues. This indicates that the leading mode is always generated. We do not discuss the origin of the leading mode here, but it may be generated by some nonlinear processes (e.g., Fuchs et al. 2005; D’Onghia et al. 2013). The overall evolution of spiral arms cannot be obtained by the linear theory. However, the linear theory can often capture some aspects of the basic physics. If we assume that the spiral arm corresponds to the most amplified wave that is predicted by the linear theory, it is expected that the shape of spiral arms can be explained by the linear theory.

We investigate the pitch angle dependence on the shear rate using the linear theory (Julian & Toomre 1966). We focus on a single wavelet with k_x , k_y , and density amplitude D . Due to the shear, the normalized radial wavenumber $\tilde{k}_x = k_x/(2\pi/\lambda_{\text{cr}})$ increases with time \tilde{t}

$$\tilde{k}_x(\tilde{t}) = \frac{\Gamma \tilde{k}_y \tilde{t}}{\tilde{\kappa}}, \quad (18)$$

where \tilde{t} is the normalized time $\tilde{t} = t\kappa$, and \tilde{k}_y is the normalized azimuthal wavenumber $\tilde{k}_y = k_y/(2\pi/\lambda_{\text{cr}})$ that is the inverse of X in Julian & Toomre (1966): $\tilde{k}_y = 1/X$, while $\tilde{\kappa}$ is constant. The wavelet is trailing when $\tilde{t} > 0$ ($\tilde{k}_x > 0$) and leading when $\tilde{t} < 0$ ($\tilde{k}_x < 0$).

As the wavelet rotates, the density amplitude D varies with \tilde{t} . The density amplitude evolution is given by the integral equation (Julian & Toomre 1966):

$$D(\tilde{t}) = \int_{\tilde{t}_i}^{\tilde{t}} K(\tilde{t}', \tilde{t}; \kappa, Q, \tilde{k}_y)(D_{\text{imp}} + D(\tilde{t}'))d\tilde{t}', \quad (19)$$

where K is the kernel function, and D_{imp} is the density amplitude by the imposed perturbation.

We consider the wavelet excited at the initial time $\tilde{t} = \tilde{t}_i$ due to some disturbance, and neglect any disturbance to the wavelet after $\tilde{t} = \tilde{t}_i$, that is, we assume $D_{\text{imp}} = 0$ for $t > t_i$. From Equation (18), \tilde{t}_i is related to the initial radial wave number $\tilde{k}_{xi} = \Gamma \tilde{k}_y \tilde{t}_i / \tilde{\kappa}$. Therefore, the solution to the integral equation $D(\tilde{t})$ depends on the four dimensionless parameters $\tilde{\kappa}$, Q , \tilde{k}_{xi} and \tilde{k}_y . The two parameters $\tilde{\kappa}$ and Q stand for a disk model, and the other two parameters \tilde{k}_{xi} and \tilde{k}_y specify the wavelet that we focus on.

The typical solution is shown in Figure 5. The parameters are $\tilde{\kappa} = 1.4$, $Q = 1.2$, $\tilde{k}_{xi} = -1.82$, and $\tilde{k}_y = 0.5$. The solution has the maximum value $D_{\text{peak}} = 38.8$ at the positive time $\tilde{t}_{\text{peak}} = 6.10$, which means that the wavelet is trailing when the wavelet is most amplified. The peak amplitude D_{peak} sensitively depends on the wavelet. In the case where we fix $\tilde{\kappa}$ and Q , the peak amplitude has the maximum value D_{max} at \tilde{t}_{max} for $\tilde{k}_{xi} = \tilde{k}_{xi, \text{max}}$ and $\tilde{k}_y = \tilde{k}_{y, \text{max}}$. Figure 6 shows the dependence of D_{peak} on \tilde{k}_{xi} and \tilde{k}_y . For $\tilde{\kappa} = 1.4$ and $Q = 1.2$, the maximum amplitude is $D_{\text{max}} = 44.8$ at $\tilde{t}_{\text{max}} = 5.65$ for $\tilde{k}_{xi, \text{max}} = -2.2$ and $\tilde{k}_{y, \text{max}} = 0.60$.

We assume that wavelets with any wavenumbers always exist because of the density fluctuation. The particular wavelet with $\tilde{k}_{xi, \text{max}}$ and $\tilde{k}_{y, \text{max}}$ is amplified most extensively. Its amplitude becomes D_{max} times larger than the initial amplitude at the positive time \tilde{t}_{max} . We interpret the most

amplified wavelet as the spiral structures observed in the simulation. The corresponding pitch angle is calculated from \tilde{t}_{\max} . From Equation (14), \tilde{t}_{\max} is related to the pitch angle:

$$\tan \theta_{\max} = \frac{\tilde{\kappa}}{\Gamma \tilde{t}_{\max}}. \quad (20)$$

The values D_{\max} and \tilde{t}_{\max} depend on the disk parameters $\tilde{\kappa}$ and Q . Figure 7 shows \tilde{t}_{\max} and D_{\max} as a function of $\tilde{\kappa}$ and Q . The maximum amplitude D_{\max} depends on Q sensitively. This is consistent with the results of the N -body simulations. The right panel of Figure 7 shows \tilde{t}_{\max} , where \tilde{t}_{\max} slightly decreases with Q and is roughly constant value $\simeq 3.5$ for $Q \gtrsim 1.5$.

Since Q changes with time in the simulations, we cannot use Q_{ini} to calculate the pitch angle. Figure 8 shows the time evolution of Q . The Q value increases more rapidly for smaller $\tilde{\kappa}$ and initial Q value. Thus, for $\kappa \lesssim 1.4$, although the initial Q is less than 1.5, the final Q becomes 1.5 - 2.0. Therefore in estimating the pitch angle, we can assume $Q > 1.5$ independent of Q_{ini} . As discussed above, \tilde{t}_{\max} is roughly constant $\simeq 3.5$ independent of $\tilde{\kappa}$ and Q for $Q > 1.5$. Thus, from Equation (20), the pitch angle is estimated as

$$\tan \theta_{\max} = \frac{\kappa}{6.9A}, \quad (21)$$

which agrees well with the fitting formula obtained from the numerical simulations, Equation (15).

Strictly speaking, for $Q_{\text{ini}} < 1.4$ and $\tilde{\kappa} \gtrsim 1.6$ ($\Gamma \lesssim 0.5$), we cannot use that $Q \gtrsim 1.5$ and Equation (21). In fact, Equation (21) for large κ (small Γ) has larger error than that for small κ (large Γ). However, Equation (21) for small Γ explain the general trend of the dependence on Γ .

5. Conclusion

We performed the local N -body simulations of stellar disks and calculated the pitch angle θ of the spiral arms as a function of the shear rate Γ . We found that θ is well fitted by Equation (15), which agrees well with the observational results (Seigar et al. 2006). The pitch angle θ decreases with Γ . For large Γ or small κ , the winding due to the shear is so effective that θ is small.

We also calculated the time evolution of the wavelet amplitude using the liner theory (Julian & Toomre 1966). The leading wavelet rotates and is amplified owing to the swing amplification mechanism (Toomre 1981; Toomre & Kalnajs 1991). The spiral arm can be interpreted as the wavelet amplified by this mechanism. We calculated the time when the density amplitude is maximum and θ at that time. If Toomre's Q value is larger than 1.5, θ is approximately given by Equation (21). Although the initial Q is small, Q increases rapidly due to heating by the spiral arms and exceeds 1.5 finally. Thus, θ calculated by the numerical simulations agrees with Equation (21). All these results suggest that the spiral arms in this simulation are formed by the swing amplification from the leading wavelet in the density fluctuation.

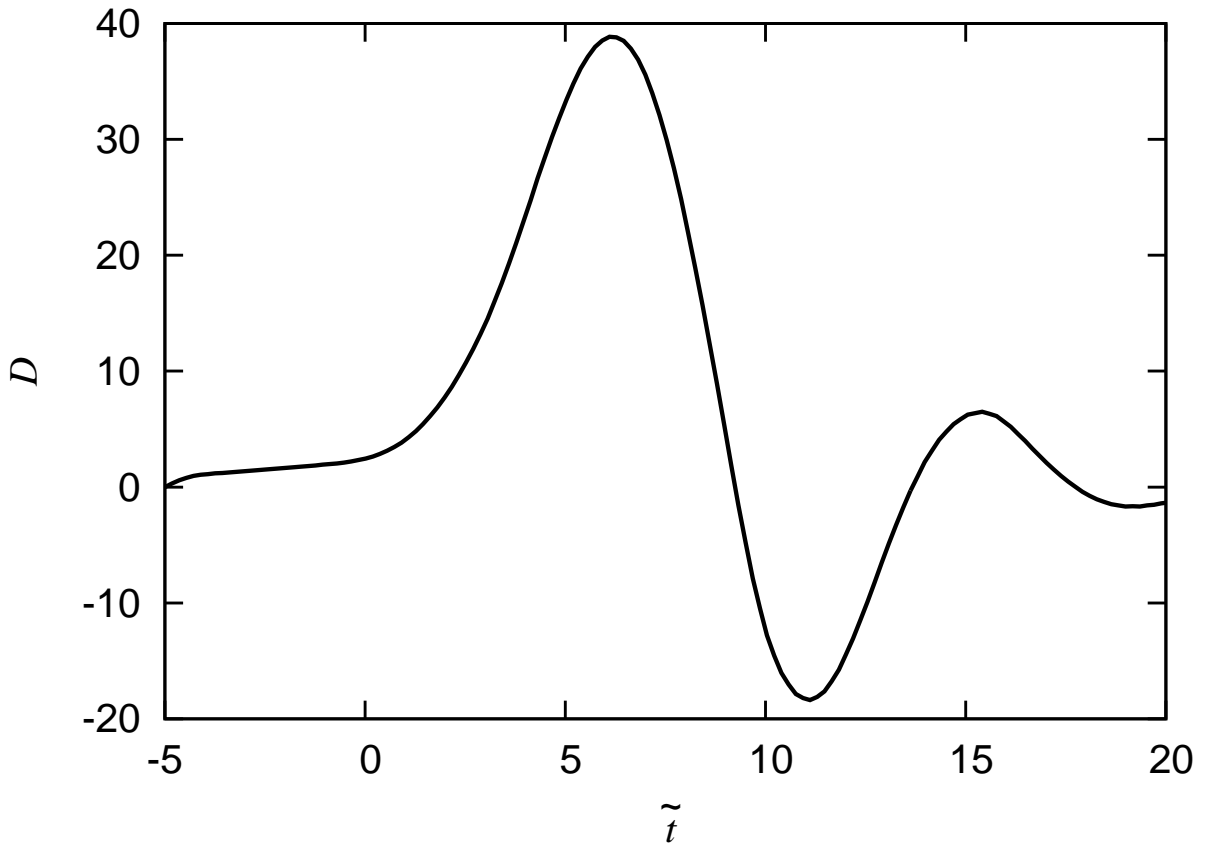


Fig. 5.— The time evolution of the wavelet amplitude D calculated by the linear theory for $\tilde{\kappa} = 1.4$, $Q = 1.2$, $\tilde{k}_{xi} = -1.82$ ($\tilde{t}_i = -5.0$), and $\tilde{k}_y = 0.5$.

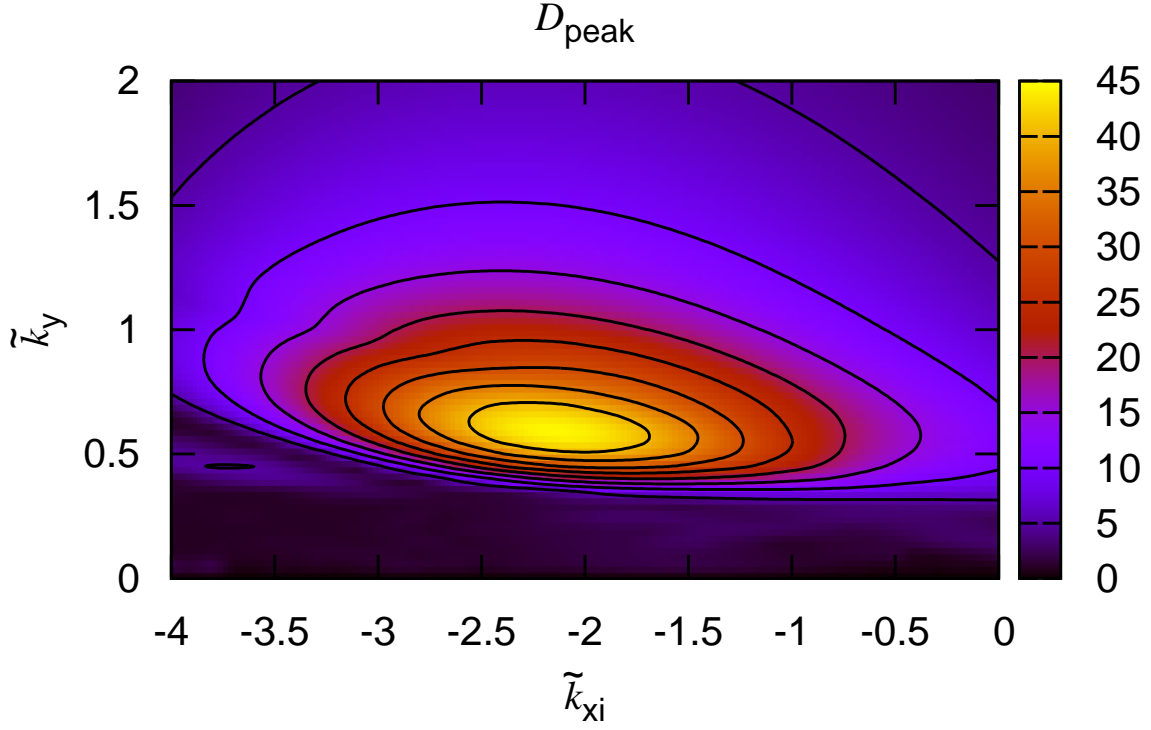


Fig. 6.— The peak amplitude D_{peak} as a function of \tilde{k}_{xi} and \tilde{k}_y for $\tilde{\kappa} = 1.4$ and $Q = 1.2$.

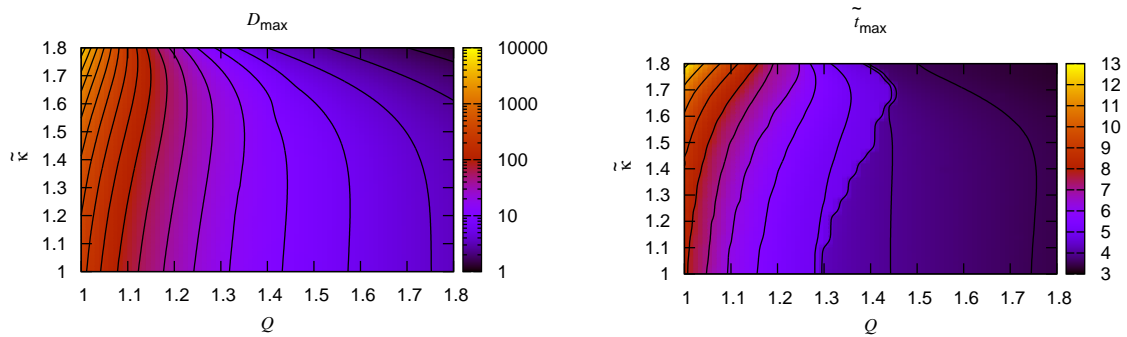


Fig. 7.— The maximum amplitude D_{max} (left panel) and the corresponding time \tilde{t}_{max} (right panel) as a function of $\tilde{\kappa}$ and Q .

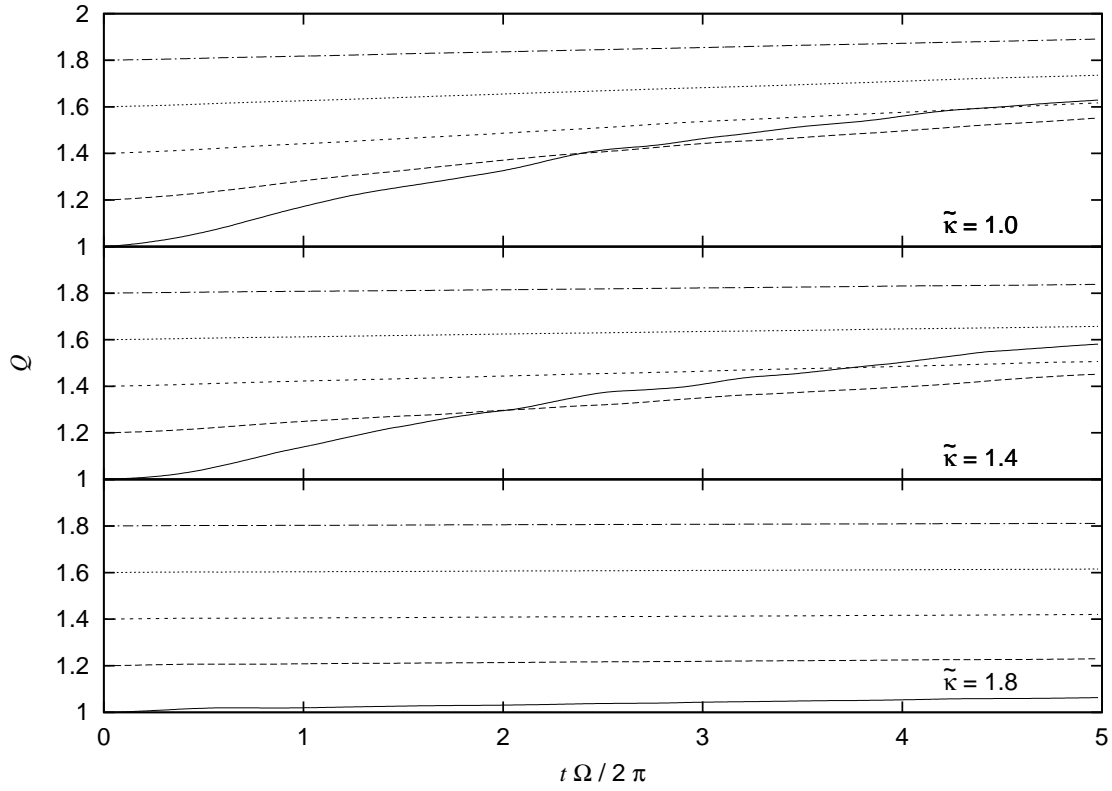


Fig. 8.— The time evolution of Toomre's Q value for the epicycle frequency $\tilde{\kappa} = 1.0$ (top), $\tilde{\kappa} = 1.4$ (middle), $\tilde{\kappa} = 1.8$ (bottom) . The initial Q value is 1.0 (solid), 1.2 (dashed), 1.4 (short-dashed), 1.6 (dotted), and 1.8 (dot-dashed).

The present simulation and linear theory employed the local approximation. We may directly apply these results to flocculent spiral galaxies. Strictly speaking, we should not apply these results to grand-design spiral galaxies. However, we expect that these results are useful for understanding the basic physics of spiral arms in general.

In recent years, it was found that the nonlinear effect is significant to understand the overall activity of the spiral arms (e.g., Baba et al. 2013; D’Onghia et al. 2013). We found that the linear theory can predict the correct pitch angle that is consistent with the numerical simulation. This indicates that the linear theory is still useful to explain the shape of the spiral arms. We will investigate the non-linear process of spiral arm formation by gravitational instability in more detail in the future work.

Numerical computations were carried out on GRAPE system at Center for Computational Astrophysics, National Astronomical Observatory of Japan.

REFERENCES

- Baba, J., Asaki, Y., Makino, J., Miyoshi, M., Saitoh, T. R., & Wada, K. 2009, *ApJ*, 706, 471
- Baba, J., Saitoh, T. R., & Wada, K. 2013, *ApJ*, 763, 46
- Binney, J., & Tremaine, S. 2008, *Galactic Dynamics: Second Edition*, by James Binney and Scott Tremaine. ISBN 978-0-691-13026-2 (HB). Published by Princeton University Press, Princeton, NJ USA, 2008.
- Buta, R., Vasylyev, S., Salo, H., & Laurikainen, E. 2005, *AJ*, 130, 506
- D’Onghia, E., Vogelsberger, M., & Hernquist, L. 2013, *ApJ*, 766, 34
- French, R. G., Salo, H., McGhee, C. A., & Dones, L. 2007, *Icarus*, 189, 493
- Fuchs, B. 2001, *A&A*, 368, 107
- Fuchs, B., Dettbarn, C., & Tsuchiya, T. 2005, *A&A*, 444, 1
- Fujii, M. S., Baba, J., Saitoh, T. R., Makino, J., Kokubo, E., & Wada, K. 2011, *ApJ*, 730, 109
- Gammie, C. F. 2001, *ApJ*, 553, 174
- Goldreich, P. & Lynden-Bell, D. 1965, *MNRAS*, 130, 125
- Grand, R. J. J., Kawata, D., & Cropper, M. 2013, *A&A*, 553, A77
- Ida, S., Kokubo, E., & Makino, J. 1993, *MNRAS*, 263, 875
- Julian, W. H. & Toomre, A. 1966, *ApJ*, 146, 810

- Kawai, A., & Fukushige, T. 2006, Proc. 2006 ACM/IEEE Conf. on Supercomputing
- Kokubo, E. & Ida, S. 1992, PASJ, 44, 601
- Lin, C. C. & Shu, F. H. 1964, ApJ, 140, 646
- . 1966, Proceedings of the National Academy of Science, 55, 229
- Oh, S. H., Kim, W.-T., Lee, H. M., & Kim, J. 2008, ApJ, 683, 94
- Salo, H. 1992, Nature, 359, 619
- . 1995, Icarus, 117, 287
- Salo, H. & Schmidt, J. 2010, Icarus, 206, 390
- Seigar, M. S., Block, D. L., Puerari, I., Chorney, N. E., & James, P. A. 2005, MNRAS, 359, 1065
- Seigar, M. S., Bullock, J. S., Barth, A. J., & Ho, L. C. 2006, ApJ, 645, 1012
- Sellwood, J. A. 2000, Ap&SS, 272, 31
- . 2010, ArXiv e-prints
- Sellwood, J. A. & Carlberg, R. G. 1984, ApJ, 282, 61
- Toomre, A. 1964, ApJ, 139, 1217
- Toomre, A. 1981, Structure and Evolution of Normal Galaxies, 111
- Toomre, A., & Kalnajs, A. J. 1991, Dynamics of Disc Galaxies, 341
- Toomre, A. & Toomre, J. 1972, ApJ, 178, 623
- Wakita, S. & Sekiya, M. 2008, ApJ, 675, 1559
- Wisdom, J., & Tremaine, S. 1988, AJ, 95, 925